

Article

Design and Experimental Investigation of a Piezoelectric Rotation Energy Harvester Using Bistable and Frequency Up-Conversion Mechanisms

Zhengqiu Xie ¹, Jitao Xiong ¹, Deqi Zhang ¹, Tao Wang ², Yimin Shao ¹ and Wenbin Huang ^{1,*} 

¹ The State Key Lab of Mechanical Transmissions, Chongqing University, Chongqing 400044, China; zhengqiuxie@163.com (Z.X.); jitaotielan@163.com (J.X.); 13370720664@163.com (D.Z.); ymshao@cqu.edu.cn (Y.S.)

² China North Vehicle Research Institute, Beijing 100072, China; tonywangbj@aliyun.com

* Correspondence: whuang@cqu.edu.cn; Tel.: +86-185-8006-9763

Received: 13 July 2018; Accepted: 17 August 2018; Published: 21 August 2018



Abstract: Harvesting energy from rotational motion for powering low-power electrical devices is attracting increasing research interest in recent years. In this paper, a magnetic-coupled buckled beam piezoelectric rotation energy harvester (MBBP-REH) with bistable and frequency up-conversion is presented to harvest low speed rotational energy with a broadband. A buckled beam attached with piezoelectric patches under dynamical axial load enables the harvester to achieve high output power under small excitation force. The electromechanical coupling dynamical model is developed to characterize the MBBP-REH. Both the simulations and experiments are carried out to evaluate the performance of the harvesters in various conditions under different excitations. The experimental results indicate that the proposed harvester is applicable for low speed rotation and can generate stable output power under wideband rotating excitation. For the harvester with two magnets that produce attractive forces with the center magnet of the buckled beam, the average power is 682.7 μW and the maximum instantaneous power is 1450 μW at 360 r/min.

Keywords: rotational energy harvesting; buckled beam; bistable; frequency up-conversion; magnetic plucking

1. Introduction

With the development of low-power and low-cost electronic devices, these devices are extensively used in civil, industrial, and military areas. Furthermore, these devices are primarily powered by batteries, which have the weaknesses of high replacement cost, limited life time, and environmental pollution. Thus energy supply becomes a prominent problem that needs to be solved urgently. Energy harvesting from ambient environment is regarded as a promising means to replace conventional batteries or extend the lifetime of batteries for powering low-power electronic devices. A variety of energy harvesting devices have been proposed to harness mechanical energy including vibration, airflow, ocean waves, rotation, and human motion, which is widely distributed in environment. Piezoelectric [1,2], electromagnetic [3,4], electrostatic [5], and triboelectric [6] are the main transaction mechanisms used to convert mechanical energy into electrical energy.

Considering the traditional linear energy harvesters are unable to harvest energy from broadband excitations or excitations with time-varying frequency. Nonlinear energy harvesters have been developed to overcome the above shortcomings of the linear harvesters. Monostable and bistable harvesters are the typical structures for nonlinear energy harvesting. For monostable energy harvester, Fan et al. [7] developed a monostable piezoelectric energy harvester by applying a symmetric magnetic

attraction and a pair of stoppers, which can harvest vibration energy from low-level excitations. Nasser et al. [8] proposed an efficient and broadband vortex-induced vibrations energy harvester by using nonlinear attractive magnetic forces.

As another class of nonlinear harvesters, bistable energy harvesters have also been investigated extensively. Double potential wells of the potential function is the critical feature of these devices, which can realize the inter-well oscillation to dramatically improve the vibration displacement and velocity. Magnetic forces [9,10], residual stresses that are produced by fabrication process [11], or axial preloaded [12–14] are the main methods to achieve bistability. Erturk et al. [15] investigated a piezomagnetoelastic energy harvester using a piezoelectric ferromagnetic beam and external magnets to enhance the operation bandwidth and the output power. A bistable inertial harvester comprised of a piezoelectric cantilever with a tip magnet and a fixed magnet is proposed by Stanton et al. [9]. Arrieta et al. [16] designed a piezoelectric bistable plate harvester utilizing a bistable composite plate with attached piezoelectric patches to realize large amplitude vibrations and a wide response bandwidth. For axial preload bistable energy harvesters, Leland and Wright [17] proposed a tunable-resonance vibration energy harvester using an axial preload to the piezoelectric bimorph for adjusting its resonance frequency. A comprehensive understanding of the axial preload piezoelectric harvester was developed by Masana and Daqaq [18]. In order to enhance the output voltage-amplitude and broaden the frequency response bandwidth at low frequencies and small axial excitations, a magnet-coupled buckled-beam piezoelectric harvester was developed by Zhu and Zu [19]. Further, an elastic clamp boundary with axial compressive effects and compliant suspensions were developed in order to improve the average power and bandwidth of the buckled piezoelectric beam harvesters [14,20]. Zhang et al. [21] designed a wind energy harvester using the buckled beam to enhance the output performance. Jiang et al. [22] proposed a multi-step buckled beam piezoelectric energy harvester to obtain a wide operational bandwidth. Gafforelli et al. [23] presented a bridge shaped nonlinear energy harvester to widen the frequency bandwidth significantly.

In consideration of stochastic, multi-frequencies, and time-varying motions, frequency up-conversion using direct impact or non-contact magnetic plucking can be another solution. In order to adapt to the low-frequency and high-amplitude features of human motion, Renaud et al. [24] designed an impact harvester with a moving mass and piezoelectric bending structures. Wei et al. [25] developed an impact-driven piezoelectric energy harvester to realize frequency up-conversion from human motion. In order to avoid the mechanical collision and increase the durability of the harvesters, Tang et al. [26] developed a miniature piezoelectric energy harvester using magnetic repulsive forces to realize the non-contact frequency up-conversion. Pillatsch et al. [27] designed an inertial energy harvesting device utilizing rotating proof mass to achieve piezoelectric beam plucking through magnetic coupling. Ramezanpour et al. [28] theoretically and experimentally investigated a vibration-based energy harvester with a rotating magnetic proof mass and piezoelectric bimorph beams.

In comparison with linear motion, rotational motion is more widely existing in civil and industrial environments, such as wheels, tires, rotating machines, shafts, gas, and wind turbines, etc. Thus, energy harvesting from rotational motion to powering low-power electrical device is promising and achievable. Nonlinear vibration energy harvesters design reviewed above can be employed to harvest rotational energy. Depending on whether the whole structure or only the excitation source is rotational, rotational energy harvesters can be divided into two categories: rotating energy harvesters and rotation-excitation energy harvesters. For rotating energy harvesters, the whole device is under rotation. A compact, passive self-tuning rotational energy harvester comprising of a relatively rigid piezoelectric beam and a narrow, flexible driving beam with a tip mass is proposed by Gu and Livermore [29]. Guan and Liao [30] proposed a rotational piezoelectric energy harvester with a tip mass at the rotating center to reduce the centrifugal force. Febbo et al. [31] designed a rotational energy harvesting system that consists of a primary piezoelectric elastic beam, an elastic beam, and two heavy masses jointed by a spring for low speed rotation applications. On the other side, rotation-excitation energy harvesters

are designed to be composed of a non-rotational harvesting part and a rotational excitation source. Karami et al. [32] proposed a piezoelectric transducer using bistable piezoelectric bimorphs for low speed wind energy harvesting. Kan et al. [33] presented a piezo-windmill that is excited by rotating magnets to harvest low and wide range wind speed. Fu and Yeatman [34] developed a rotational harvester with bi-stability and frequency up-conversion to harness low rotation speed kinetic energy with a wide bandwidth. Zou et al. [35] designed a magnetically coupled flextensional rotation energy harvester that consists of flextensional transducers and rotating magnets. Xie et al. [36] proposed a rotational energy harvester and the corresponding experimental results showed that it could harvest wideband low-speed rotational energy.

Nonlinear energy harvesting mechanism and frequency up-conversion are widely used in the design of energy harvesters. However, rare work has been proposed by combining multiple nonlinear mechanisms together for rotation energy harvesting, which is supposed to exhibit better performance. In order to optimize the structure and enhance the performance of the rotational energy harvester in [33], a magnetic axial coupling structure with an optimized magnetic frequency up-conversion mechanism is proposed in this paper. Therefore, a magnetic-coupled buckled beam piezoelectric rotational energy harvester (MBBP-REH) is designed for low speed rotational energy harvesting with a wide response bandwidth. This paper theoretically and experimentally investigated the dynamical characteristics of the improved rotational energy harvester. The characteristic responses of different design parameters are presented in this paper. The paper is organized as follows: In Section 2, the design is presented and the mathematical model is developed. The experiment setup is described in Section 3. Section 4 presents the results and discussion. The summary is concluded in Section 5.

2. Design and Modeling

2.1. Design

The MBBP-REH with dynamic axial load for rotational energy harvesting is shown schematically in Figure 1. The excitation magnets are arranged to have the same or alternative parallelity along the circumference. For the parallel arrangement, the excitation magnets can be in phase (Figure 1a) or out-of-phase (Figure 1b) with the center magnet on the buckled beam. The arrangement with alternative parallelity is shown in Figure 1c. The excitation magnets are attached to the revolving host. The buckled beam is made of bronze substrate that is partly covered with two serially connected piezoelectric patches at one end. One end of the beam is clamped and fixed, while the other end carries a moving mass and a magnet, thus it can move along the axial direction under the dynamic axial load. A magnet with the opposite magnetism direction is fixed on the frame facing to the moving mass, with a small clearance between each other. The interaction force between these two magnets enables the initial buckling state of the beam. By adjusting the initial gap between two magnets, different initial buckling states can be established.

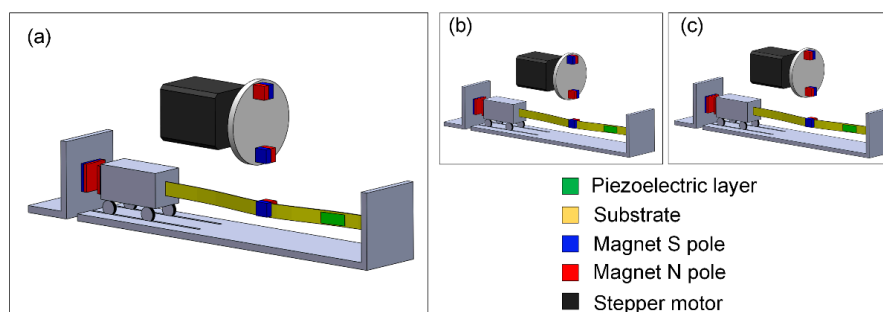


Figure 1. Schematics of the magnetic-coupled buckled beam piezoelectric rotational energy harvester (MBBP-REH), the rotational excitation magnets are arranged to have the same ((a) in phase or (b) out-of-phase with the center magnet) or alternative (c) parallelity along the circumference.

2.2. Modeling

The electromechanical coupling dynamical model can be formulated while using the extended Hamilton’s method. The kinetic energy of the MBBP-REH can be given by

$$T = \frac{1}{2} \int_0^l m_{pb} (\dot{u}(x,t)^2 + \dot{w}(x,t)^2) dx + \frac{1}{2} m_c \left(\dot{u} \left(\frac{l}{2}, t \right)^2 + \dot{w} \left(\frac{l}{2}, t \right)^2 \right) + \frac{1}{2} m_a \dot{u}(l,t)^2 \quad (1)$$

where m_{pb} is the mass per unit length of the buckled beam, and it can be given as $m_{pb} = r_s b_s h_s + r_p b_p h_p [H(x - l_1) + H(x - l_1 - l_p)]$, ρ_s and ρ_p are the density of the substrate and the piezoelectric patches, b_s and b_p are the width of the substrate and the piezoelectric patches, h_s and h_p are the thickness of the substrate and the piezoelectric patches, l_1 and l_p are the location and the length of the piezoelectric patches, $H(x)$ is the Heaviside function, m_c is the mass of the center magnet, m_a is the mass of the end moving mass with a magnet, $w(x, t)$ and $u(x, t)$ are the transverse and longitudinal displacement of the buckled beam, and the superscript dot represents the derivative with respect to the time, and l is the length of the buckled beam.

The potential energy of the buckled beam is expressed as

$$U = \frac{1}{2} \int_0^l EI (w'')^2 dx - J_p V(t) \int_0^{l_p} w'' dx + \frac{1}{2} C_p V(t)^2 \quad (2)$$

where ($'$) denotes the derivative with respect to location x , J_p is the electromechanical coupling term, which can be given as $J_p = d_{31} E_p b_p h_p (h_s h_p + h_p^2) / (2h_p) [H(x - l_1) - H(x - l_1 - l_p)]$, where d_{31} is the piezoelectric strain constant. $C_p = \epsilon_{33}^S b_p l_p / (2h_p)$ is the capacitance of the piezoelectric patches, where ϵ_{33}^S is the permittivity at constant strain. $V(t)$ is the generated voltage of the piezoelectric patches. The bending stiffness is given by

$$EI = \frac{E_s b_s h_s^3}{12} [H(x) - H(x - l_1) + H(x - l_1 - l_p)] + \frac{E_s b_s h_s^3 + 2E_p b_p (3h_s^2 h_p + 6h_s h_p^2 + 4h_p^3)}{12} [H(x - l_1) - H(x - l_1 - l_p)] \quad (3)$$

where E_s and E_p are the Young’s modulus of the elastic beam and the piezoelectric layers, respectively.

The magnets that are used in the harvester can be modeled as point dipoles by following the reference [37]. The distance \mathbf{r}_i from the i th rotational magnet to the center magnet can be given as

$$\mathbf{r}_i = (R \sin \beta_i - w) \hat{\mathbf{e}}_x - (R - R \cos \beta_i + d) \hat{\mathbf{e}}_y \quad (4)$$

where R is the rotational radius of excitation magnets, β_i is the angular displacement of the excitation magnet E_i , and d is the minimum center distance between the excitation magnets and the center magnet along the y direction.

For the center magnet attached to the buckled beam, the magnetic moment vectors can be expressed as

$$\boldsymbol{\mu}_C = M_C V_C \hat{\mathbf{e}}_x \quad (5)$$

where M_C is the magnitude of the magnetization vector, and can be calculated as $M_C = B_r / u_0$ where B_r is the residual flux density of the magnet and u_0 is the permeability of free space. V_C is the volume of the magnet C. As shown in Figure 2, it can be found that the interaction forces between excitation magnets and center magnet are attractive force, and the magnetic moment vectors $\boldsymbol{\mu}_i$ of excitation magnets E_i can be given by

$$\boldsymbol{\mu}_i = (-1)^N (M_E V_E \cos \beta_i \hat{\mathbf{e}}_x + M_E V_E \sin \beta_i \hat{\mathbf{e}}_y) \quad (6)$$

where $N = 0$ represents the circular parallel and in phase arrangement with the attractive interaction forces between the excitation magnets and center magnet, $N = 1$ represents the circularly parallel and

out-of-phase arrangement with the repulsive interaction forces between the excitation magnets and center magnet, and $N = i - 1$ represents the arrangement with alternative parallelity where attractive and repulsive forces occurs alternatively. M_E is the magnitude of the magnetization vector and it can be calculated as $M_E = B_r/u_0$. V_E is the volume of the magnet E_i , and β_i can be given as $\beta_i = \beta + 2(i - 1)\pi/n$, where n is the number of the excitation magnets.

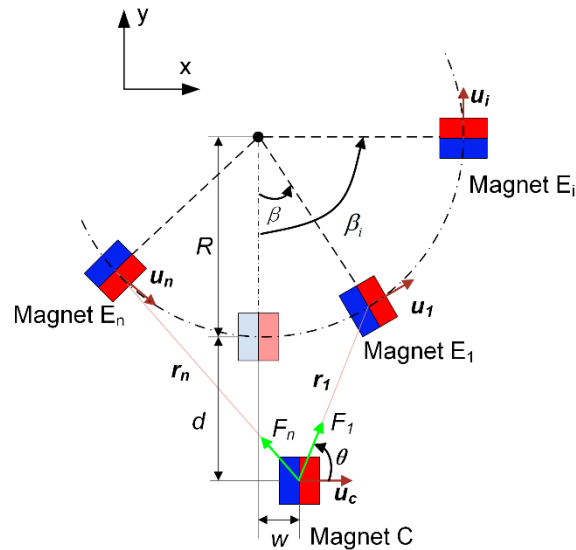


Figure 2. Schematic of dynamic analysis of the MBBP-REH with the parallelity arrangement of the excitation magnets.

The magnetic fields produced by the magnet C upon magnets E_i can be obtained as

$$\mathbf{B}_i = -\frac{\mu_0}{4\pi} \nabla \frac{\boldsymbol{\mu}_C \cdot \mathbf{r}_i}{\|\mathbf{r}_i\|_2^3} \tag{7}$$

where $\|\cdot\|_2$ and ∇ denote Euclidean norm and vector gradient operator, respectively. The overall magnetic potential energy between the excitation magnets and center magnet can be given as

$$U_{in} = -\sum_{i=1}^n \mathbf{B}_i \cdot \boldsymbol{\mu}_i \tag{8}$$

F_{ix} is the x -direction interaction force between the center magnet and the excitation magnets. F_{ix} can be calculates as

$$F_{ix} = M_i \left\{ \begin{array}{l} \frac{3(R+d-R \cos \beta_i) \cos \beta_i + (R \sin \beta_i - w) \sin \beta_i}{[(R+d-R \cos \beta_i)^2 + (R \sin \beta_i - w)^2]^{5/2}} \\ - \frac{5(R+d-R \cos \beta_i)^2 [(R+d-R \cos \beta_i) \cos \beta_i + (R \sin \beta_i - w) \sin \beta_i]}{[(R+d-R \cos \beta_i)^2 + (R \sin \beta_i - w)^2]^{7/2}} \end{array} \right\} \tag{9}$$

where $M_i = 3M_E V_E M_C V_C \mu_0 (-1)^j / (4\pi)$, $j = 1$ and 2 denote the repulsive and attractive interaction force between the center magnet and the excitation magnet, respectively.

The magnetic force applied to the buckled beam can be regarded as a concentrate force F_{in} , given as

$$F_{in} = \sum_{i=1}^n F_{ix} \tag{10}$$

The potential energy of the magnetic field between the tip magnet and the fixed magnet on the frame can be written as

$$U_m = \frac{3\mu_0}{2\pi} \left(\frac{\boldsymbol{\mu}_T \boldsymbol{\mu}_F}{\|\mathbf{r}_{TF}\|_2^3} \right) \tag{11}$$

where $\boldsymbol{\mu}_T$ and $\boldsymbol{\mu}_F$ are the magnetic moment vectors of the tip magnet and the fixed magnet, and \mathbf{r}_{TF} is the center distance from $\boldsymbol{\mu}_T$ to $\boldsymbol{\mu}_F$.

Thus, the Lagrange function of the system is defined as the difference between the kinetic energy and the potential energy

$$L = T - U - U_m \tag{12}$$

Taking into account of the primary mechanical damping, electrical damping, and input concentrate force, the virtual work done by the non-conservative force can be given by

$$\delta W = -c_1 \int_0^{l_1} \dot{w} \delta w dx - c_2 \dot{u} \delta u + Q \delta V + F_m \delta w \tag{13}$$

where c_1 and c_2 are the damping coefficients to approximate the energy loss of viscous damping and frictions, and Q is the electric charge output of the piezoelectric patches. The time rate change of electric charge Q is the electric current transiting through the resistive loading R_L , and F_m is the interaction force between the center magnet and excitation magnets, which is regarded as the input force for the buckled beam system.

The transverse deflection of the buckled beam can be approximated using the model expression in the form of

$$w(x, t) = \sum_{n=1}^{\infty} \phi_n(x) p_n(t) \tag{14}$$

The axial deflection is related to the transverse deflection, and it can be expressed as

$$u(x, t) = \frac{1}{2} \int_0^x w'(x, t)^2 dx \tag{15}$$

Thus, \mathbf{r}_{TF} and F_m are the distance vector and equivalent magnetic force between the tip magnet and the fixed magnet, which can be further written as

$$\mathbf{r}_{TF} = (d_0 + u(l, t)) \hat{\mathbf{e}}_x \tag{16}$$

where d_0 is the initial distance between the tip magnet and the fixed magnet. F_m can be given as

$$F_m = -\frac{3\mu_0}{2\pi} \frac{M_A V_A M_B V_B}{\left(d_0 + \frac{(\pi p)^2}{16l} \right)^4} \tag{17}$$

For the Lagrange function, p and V are selected as generalized coordinates, thus the governing equations of the system can be given from

$$\begin{aligned} \frac{d}{dt} \left(\frac{\partial L}{\partial \dot{p}} \right) - \frac{\partial L}{\partial p} &= \frac{\delta W}{\delta p} \\ \frac{d}{dt} \left(\frac{\partial L}{\partial \dot{V}} \right) - \frac{\partial L}{\partial V} &= \frac{\delta W}{\delta V} \end{aligned} \tag{18}$$

The fundamental mode shape functions of the clamped-clamped beam can be written as

$$\phi_1 = (1 - \cos(2\pi x/l))/2 \tag{19}$$

The governing equations of the piezoelectric rotational energy harvester with dynamic axial loaded can be given as

$$\begin{aligned}
 m\ddot{p} + c\dot{p} + c_f p^2 \dot{p} + \zeta p + \rho(p^2 \ddot{p} + p\dot{p}^2) + \mu F_m p + \chi V &= F_{in} \\
 \dot{V} + \kappa V &= \tau \dot{p}
 \end{aligned}
 \tag{20}$$

where

$$\begin{aligned}
 m &= \int_0^l m_{pb} \phi^2(x) dx + m_c \\
 c &= c_1 \int_0^l \phi(x) dx \\
 c_f &= c_2 \left[\int_0^l \phi'(x)^2 dx \right]^2 \\
 \zeta &= \int_0^l E_{pb} I_{pb} \phi''(x)^2 dx \\
 \rho &= \int_0^l m_{pb} \left[\int_0^x \phi'(x)^2 dx \right]^2 dx + m_c \left[\int_0^{\frac{l}{2}} \phi'(x)^2 dx \right]^2 + m_a \left[\int_0^l \phi'(x)^2 dx \right]^2 \\
 \mu &= \int_0^l \phi'(x)^2 dx \\
 \chi &= \int_0^l J_p \phi''(x) dx \\
 \kappa &= 1 / (R_L C_p) \\
 \tau &= \int_0^l J_p \phi''(x) dx / C_p
 \end{aligned}$$

3. Experiment Setup

In order to verify the model of the MBBP-REH and investigate its characteristics, corresponding experimental setups are designed.

The experiment setup of the rotational energy harvesting system is shown in Figure 3a. Figure 3b shows the prototype of the developed MBBP-REH. Three MBBP-REHs with different excitation magnets arrangement are designed and examined their performances, which are referred to as MBBP-REH1, MBBP-REH2, and MBBP-REH3, respectively. MBBP-REH1 has two excitation magnets that produce attractive force with the center magnet of the buckled beam. MBBP-REH2 has two excitation magnets that generate repulsive force with the center magnet of the buckled beam. MBBP-REH3 has two magnets which produce an attractive force and a repulsive force with the center magnet of the buckled beam, respectively. Table 1 shows the geometric dimensions and the material properties of the proposed prototype. $D = 20$ mm, $d_0 = 11.2$ mm, and $R = 25$ mm when there is no special description. The revolving host is driven by a stepper motor (SS1704A20A-01, Samsr motor) with a step angle of 1.8° . The rotation speed can be set by the computer through the stepper motor controller, and a matched driver (MD-2322, Samsr motor) is utilized to drive the stepper motor. The voltage that is generated by the rotational energy harvester is collected by a signal acquisition card (6361, NI), then transferred to the computer.

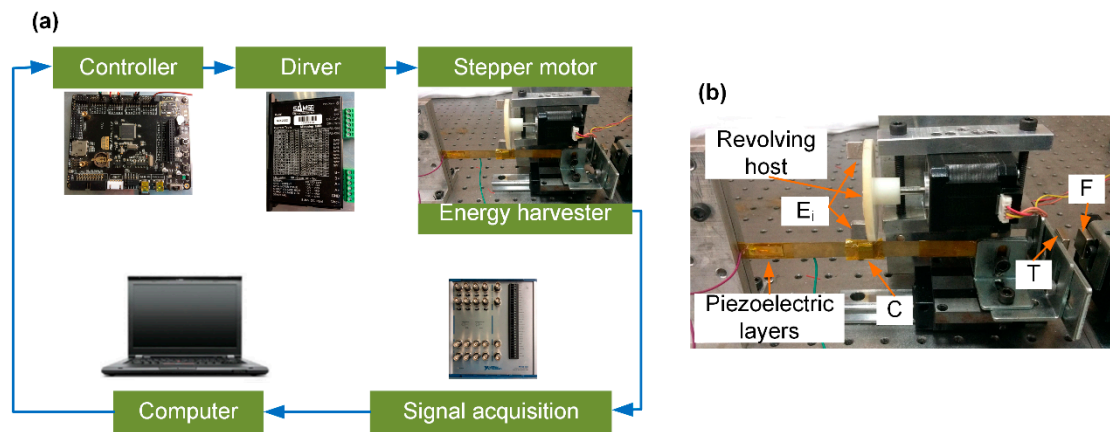


Figure 3. (a) The experiment setup and (b) the prototype.

Table 1. Material properties and geometric dimensions of the prototypes.

Parameter Description	Value
<i>Substrate</i>	
Length l	155 mm
Width b_s	10 mm
Thickness h_s	0.4 mm
Density ρ_s	8800 kg/m ³
Young's modulus E_s	110 Gpa
<i>Piezoelectric layers</i>	
Length l_p	22 mm
Width b_p	8 mm
Thickness h_p	0.24 mm
Density ρ_p	7800 kg/m ³
Young's modulus E_p	70 Gpa
Piezoelectric constant d_{31}	-285×10^{-12} C/N
Relative permittivity	3200
<i>Magnet</i>	
Dimension of tip and fixed magnets $a \times b \times c$	$15 \times 15 \times 5$ mm ³
Dimension of exciting and center magnets $A \times B \times C$	$10 \times 10 \times 10$ mm ³
Magnet's residual flux density B_r	1.2 T

4. Results and Discussion

The experiment and simulation results of the root-mean-square (RMS) open circuit voltage of MBBP-REH1 at different rotation speeds are plotted in Figure 4. In order to measure the open circuit voltage of MBBP-REH1, a load resistance of 21 MΩ was used. It is found that the simulation results are in good agreement with the experiment results. The RMS open circuit voltage of MBBP-REH1 gradually increases with the rotation speed below 240 r/min. This is owing to the more frequent occurrence of the snap-through phenomenon at higher rotation speed, resulting in a larger RMS open circuit voltage with large displacement and velocity of the buckled beam. It can be observed that the RMS open circuit voltage shows a trough around 300 r/min. This is because the buckled beam is unable to follow the input of the excitation magnets, thus the frequency of the snap-through phenomenon is reduced. As the rotation speed further increases, the buckled beam starts to snap-through more frequently and the RMS open circuit voltage increases again. Moreover, the RMS open circuit voltage gradually decreases when the rotation speed exceeds 420 r/min. The reason is that the response of the buckled beam is unable to follow up with the high frequency interaction force between the magnets, and then the buckled beam mostly vibrates around its one stable state.

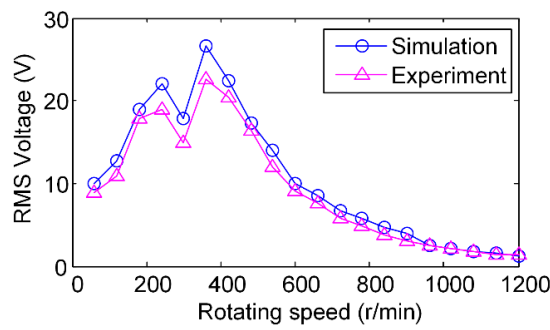


Figure 4. The root-mean-square (RMS) of the open circuit voltage of MBBP-REH1 at different rotation speeds.

The effects of the resistance loading on the average power of the MBBP-REH1 at 180 r/min, 300 r/min, and 420 r/min are shown in Figure 5, respectively. The average power can be given as $P = (V_{rms})^2 / R_L$, where V_{rms} is the root-mean-square voltage across the loading resistance R_L during a large number of periods. It can be obtained that the average power of the MBBP-REH1 first increases as the loading resistance increases, and then decreases after the loading resistance exceeds a critical value. It is shown that the average powers of MBBP-REH1 reaches its peak at 230 kΩ for 420 r/min, 280 kΩ for 300 r/min, and 390 kΩ for 180 r/min, respectively. The optimal matching resistance of the rotational energy harvester is inversely proportional to the rotation speed. In order to compare the performance of MBBP-REHs under the same conditions, the resistance of 230 kΩ is used in the following simulations and experiments.

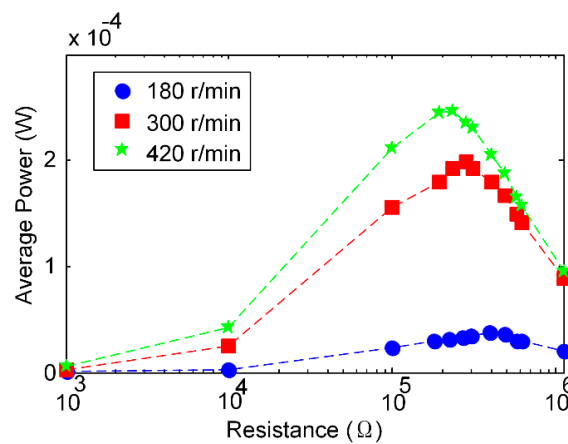


Figure 5. Effects of the resistance loading on the average powers of MBBP-REH1 at 180 r/min, 300 r/min, and 420 r/min.

The comparison of the simulation and experiment results of the output voltages of MBBP-REHs with a loading resistance of 230 kΩ for 60 r/min is shown in Figure 6. Figure 6a,d show the simulation and experiment of the output voltages of MBBP-REH1 versus time. It can be found that the voltage frequency is twice that of the rotational frequency, because there are two excitation magnets that generate attractive forces during one exciting cycle. The simulation and experiment results of MBBP-REH2 indicate two repulsive excitations in one period of rotation, as shown in Figure 6b,e. Figure 6c,f illustrate the simulation and experiment results of the output voltages of MBBP-REH3. There are an attractive force excitation and a repulsive excitation in one cycle for MBBP-REH3. With respect to the attractive force excitation, the repulsive force excitation can generate higher output voltages. This can be explained as follows. For the attractive magnet arrangement, the center magnet tends to follow with the excitation magnet as it rotates. From the other point of

view, the rotational magnet seems to drag the center magnet forward. This causes the velocity of the buckled beam to remain at a relative stable stage until the rotation angle becomes too large to maintain a high enough attraction force between two magnets. Hence, a relative flat voltage output occurs during the interaction period. In contrast, for the repulsive magnet arrangement, the beam could snap-through suddenly with a high velocity as the excitation magnet approaches, and then damps out around the far-end stable position. Therefore, a fast oscillating voltage output with high amplitude can be observed. The simulation results are in good accordance with the experiment results for different excitation magnets arrangements.

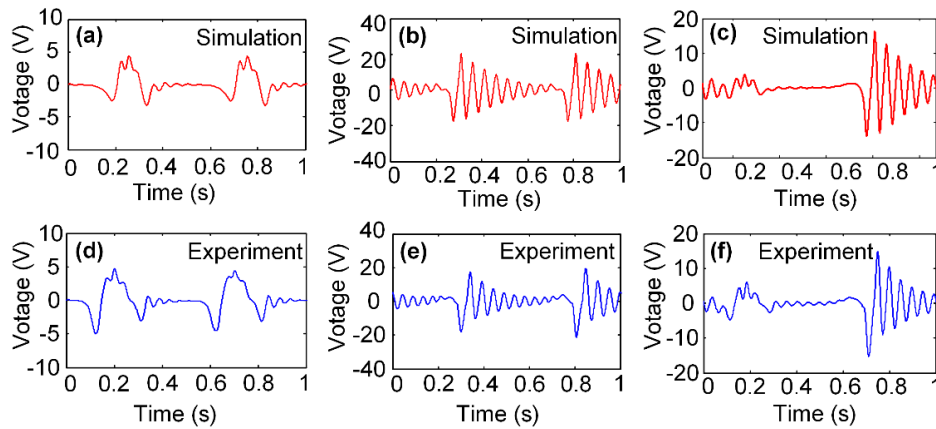


Figure 6. Comparison of the time domain waveform of the output voltages of MBBP-REH1, MBBP-REH2, and MBBP-REH3 under the rotation speed of 60 r/min: simulation (a–c) and experiment (d–f).

Figure 7 shows the comparison of the average powers of MBBP-REHs across a loading resistance of 230 kΩ under different rotation speeds. The maximum average powers of MBBP-REH1, MBBP-REH2, and MBBP-REH3 are 682.7 μW at 360 r/min, 711.7 μW at 240 r/min, and 672.2 μW at 300 r/min, respectively. It can be observed that there are two peaks for average powers of all MBBP-REHs when the rotation speed changes from 60 r/min to 600 r/min.

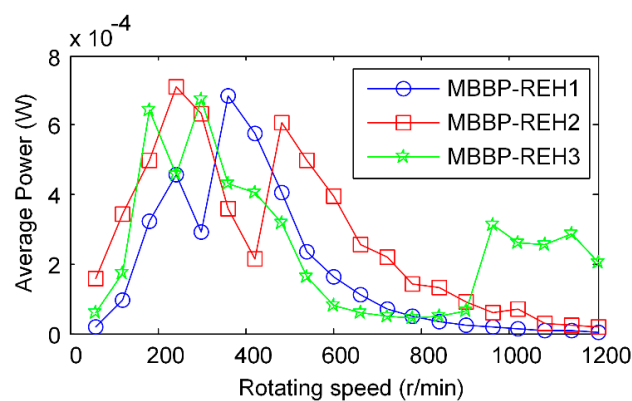


Figure 7. The comparison of the average power of MBBP-REHs across a loading resistance of 230 kΩ at different rotation speeds.

The trend of the power as a function of the rotating speed is explained, as follows. Firstly, the frequency of the snap-through phenomenon increases with the rotation speed, thus the output power increases gradually. However, for higher speeds after the first peak average power point, the beam is unable to follow the input excitation, thus the snap-through frequency and average power

decrease until the trough between two peaks. By further increasing the speed, it is observed that the snap-through frequency and the generated power increase again until the second peak point. The average power of MBBP-REH1 and MBBP-REH2 are found to gradually decrease after the rotation speed exceeds the second peak points of MBBP-REH1 and MBBP-REH2. It is due to the reason that the response of the buckled beam cannot follow up with the high frequency interaction force between the magnets, and then the buckled beam mainly vibrates around its one stable state. However, the average power of MBBP-REH3 increases and experiences a relative flat rotation speed response when the rotation speed exceeds 960 r/min. This is due to the introduction of a high frequency alternating excitation by the alternative magnets arrangement.

The time domain waveform of generated voltage of MBBP-REHs with a resistance of 230 k Ω are shown in Figure 8. Each graph of generated voltage in Figure 8 corresponds to one unique point in Figure 7. From Figure 8a–c,g–i, it is found that frequent snap-through behaviors occur at the two peaks in Figure 7. Figure 8d–f show the reduction of the snap-through frequency at suppressive rotation speeds in Figure 7. It is clearly found that the output voltage of MBBP-REH3 is larger than MBBP-REH1 and MBBP-REH2 at rotation speed of 1080 r/min in Figure 8j–l.

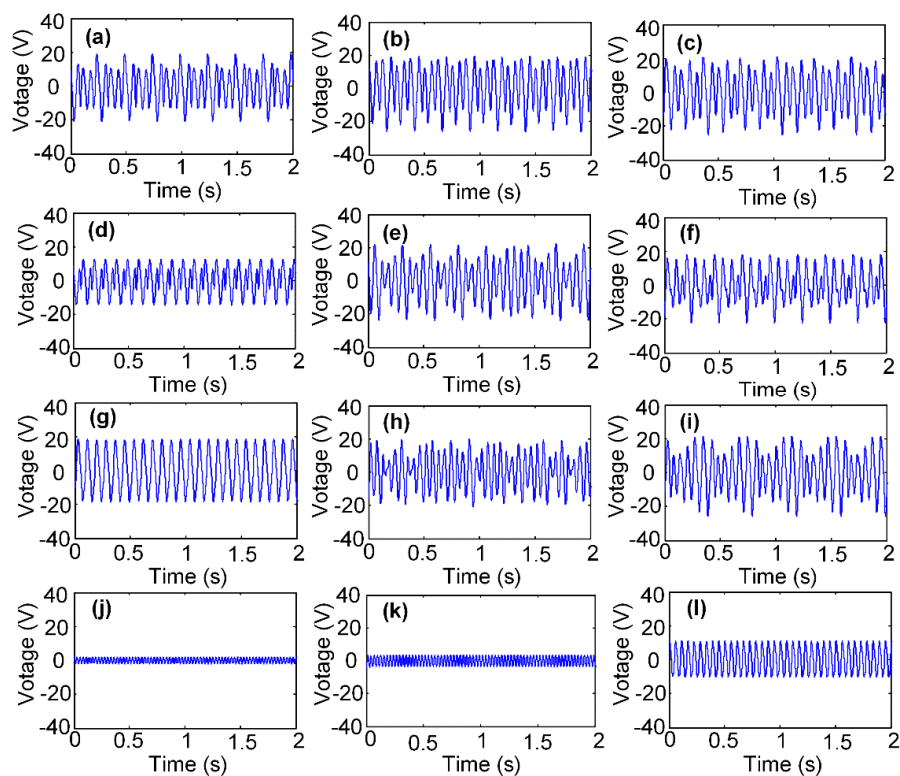


Figure 8. The time domain waveform of the output voltages of MBBP-REHs under different rotation speeds. MBBP-REH1: (a) 240 r/min; (d) 300 r/min; (g) 360 r/min; (j) 1080 r/min; MBBP-REH2: (b) 240 r/min; (e) 480 r/min; (h) 540 r/min; (k) 1080 r/min; MBBP-REH3: (c) 180 r/min; (f) 240 r/min; (i) 300 r/min and (l) 1080 r/min.

The average power of MBBP-REH1 across the loading resistance of 230 k Ω at different rotation speeds for different initial gaps between the tip magnet and the fixed magnet is shown Figure 9. The first and second resonant behaviors of average power of MBBP-REH1 are found at 360 r/min (6 Hz) and 780 r/min (13 Hz) when the attractive force between the tip magnet and the fixed magnet is relatively small ($d_0 = 24.6$ mm). Resonant peaks shift to the left and become closer as d_0 changes from 24.6 mm to 11.2 mm. It can be found that there is only one resonant peak when $d_0 = 9$ mm, and the peak average power can achieve 887.3 μ W at 240 r/min.

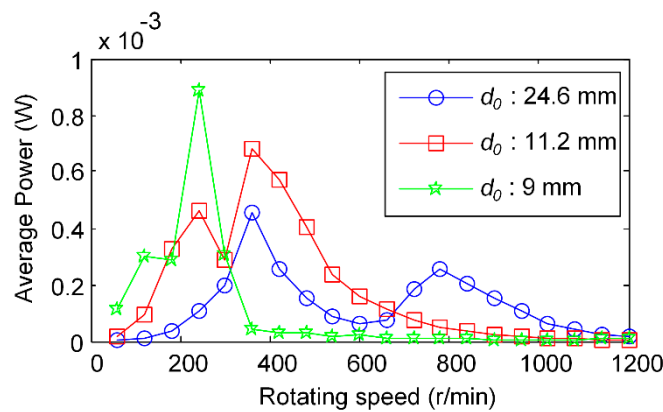


Figure 9. The average power of MBBP-REH1 at different rotation speeds for different initial gaps between the tip magnet and the fixed magnet: $d_0 = 24.6$ mm, $d_0 = 11.2$ mm, and $d_0 = 9$ mm.

The average power of MBBP-REH1 for the loading resistance of 230 kΩ with different excitation distances is shown in Figure 10. It can be observed that the average power of MBBP-REH1 increases significantly as the excitation distance (d) decreases. Meanwhile, the speed gap between the first and second resonant peaks reduces when the excitation distance decreases. The average power is 682.7 μW and the maximum instantaneous power can reach 1450 μW at 360 r/min as $d = 20$ mm. The interaction force between excitation magnets and center magnet increases as the excitation distance decreases, as a result the harvested energy increases significantly.

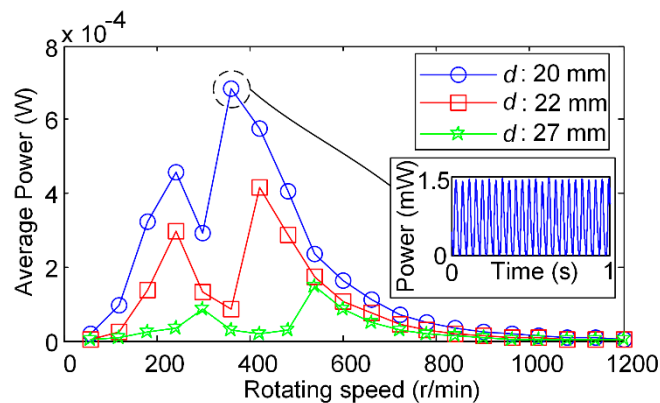


Figure 10. The average power of MBBP-REH1 at different rotation speeds for different exciting distance between the excitation magnets and the center magnet: $d = 20$ mm, $d = 22$ mm, and $d = 27$ mm.

The provided rotational energy harvester is suitable for wide bandwidth rotation speed when the design parameters are selected appropriately. Meanwhile, different excitation conditions and design parameters are investigated to analyze the output characteristics of the developed harvester. It can be found that the proposed harvester can harvest vibration energy from multiple rotation speed bands, as shown in Figure 7.

5. Conclusions

This paper presents a magnetic-coupled buckled beam piezoelectric energy harvester for rotational excitation. The electromechanical coupling dynamical model is established by the energy method based on the Hamilton’s principle. The performances of the rotational energy harvesters are evaluated by several experiments. The results demonstrate that the established mathematical model can accurately represent the characteristics of the MBBP-REHs under various excitation condition and

different configurations. The output performance is associated to the distance between tip magnet and fixed magnet, the excitation force, and excitation frequency. Appropriate distance between tip magnet and fixed magnet, and smaller excitation distance, can promote the harvested energy significantly. The experiments show the maximum average powers of MBBP-REH1, MBBP-REH2, and MBBP-REH3 can reach 682.7 μW at 360 r/min, 711.7 μW at 240 r/min, and 672.2 μW at 300 r/min, respectively. The proposed magnetic-coupled energy harvester for rotational energy harvesting can realize wide bandwidth rotation speed response, and high output performance with small excitation forces. These findings demonstrate the great potential of MBBP-REH for broadband rotational energy harvesting applications, such as tire condition monitoring, environmental monitoring, and condition monitoring of rotating machinery, etc.

Author Contributions: Z.X. established the theoretical model. Z.X., J.X. and D.Z. performed conceived and designed the experiments, Z.X. and J.X. performed the experiments, Z.X., T.W., Y.S. and W.H. analyzed the data. All authors contributed to the writing of the paper.

Funding: This research was funded by the National Natural Science Foundation of China (Grant No. 51605052 and 51605450), Fundamental Research Funds for the Central Universities (Grant No. 106112017CDJQJ118846) and Natural Science Foundation of Chongqing (Grant No. cstc2017jcyjAX0188).

Conflicts of Interest: The authors declare no conflict of interest.

References

1. Yang, Z.; Zhou, S.; Zu, J.; Inman, D. High-Performance Piezoelectric Energy Harvesters and Their Applications. *Joule* **2018**, *2*, 642–697. [[CrossRef](#)]
2. Xu, Z.; Shan, X.; Chen, D.; Xie, T. A Novel Tunable Multi-Frequency Hybrid Vibration Energy Harvester Using Piezoelectric and Electromagnetic Conversion Mechanisms. *Appl. Sci.* **2016**, *6*, 10. [[CrossRef](#)]
3. Siddique, A.R.M.; Mahmud, S.; Heyst, B.V. A comprehensive review on vibration based micro power generators using electromagnetic and piezoelectric transducer mechanisms. *Energy Convers. Manag.* **2015**, *106*, 728–747. [[CrossRef](#)]
4. Rantz, R.; Halim, M.A.; Xue, T.; Zhang, Q.; Gu, L.; Yang, K.; Roundy, S. Architectures for wrist-worn energy harvesting. *Smart Mater. Struct.* **2018**, *27*, 044001. [[CrossRef](#)]
5. Zhang, Y.; Wang, T.; Luo, A.; Hu, Y.; Li, X.; Wang, F. Micro electrostatic energy harvester with both broad bandwidth and high normalized power density. *Appl. Energy* **2018**, *212*, 362–371. [[CrossRef](#)]
6. Wu, C.; Liu, R.; Wang, J.; Zi, Y.; Lin, L.; Wang, Z.L. A spring-based resonance coupling for hugely enhancing the performance of triboelectric nanogenerators for harvesting low-frequency vibration energy. *Nano Energy* **2017**, *32*, 287–293. [[CrossRef](#)]
7. Fan, K.; Tan, Q.; Zhang, Y.; Liu, S.; Cai, M.; Zhu, Y. A monostable piezoelectric energy harvester for broadband low-level excitations. *Appl. Phys. Lett.* **2018**, *112*, 123901. [[CrossRef](#)]
8. Naseer, R.; Dai, H.L.; Abdelkefi, A.; Wang, L. Piezomagnetoelastic energy harvesting from vortex-induced vibrations using monostable characteristics. *Appl. Energy* **2017**, *203*, 142–153. [[CrossRef](#)]
9. Stanton, S.C.; McGehee, C.C.; Mann, B.P. Nonlinear dynamics for broadband energy harvesting: Investigation of a bistable piezoelectric inertial generator. *Phys. D Nonlinear Phenom.* **2010**, *239*, 640–653. [[CrossRef](#)]
10. Erturk, A.; Inman, D.J. Broadband piezoelectric power generation on high-energy orbits of the bistable Duffing oscillator with electromechanical coupling. *J. Sound Vib.* **2011**, *330*, 2339–2353. [[CrossRef](#)]
11. Emam, S.A.; Inman, D.J. A Review on Bistable Composite Laminates for Morphing and Energy Harvesting. *Appl. Mech. Rev.* **2015**, *67*, 060803. [[CrossRef](#)]
12. Masana, R.; Daqaq, M.F. Relative performance of a vibratory energy harvester in mono- and bi-stable potentials. *J. Sound Vib.* **2011**, *330*, 6036–6052. [[CrossRef](#)]
13. Kitio Kwuimy, C.A.; Litak, G.; Borowiec, M.; Nataraj, C. Performance of a piezoelectric energy harvester driven by air flow. *Appl. Phys. Lett.* **2012**, *100*, 024103. [[CrossRef](#)]
14. Harne, R.L.; Wang, K.W. Axial suspension compliance and compression for enhancing performance of a nonlinear vibration energy harvesting beam system. *J. Vib. Acoust.* **2016**, *138*, 011004. [[CrossRef](#)]
15. Erturk, A.; Hoffmann, J.; Inman, D.J. A piezomagnetoelastic structure for broadband vibration energy harvesting. *Appl. Phys. Lett.* **2009**, *94*, 254102. [[CrossRef](#)]

16. Arrieta, A.F.; Hagedorn, P.; Erturk, A.; Inman, D.J. A piezoelectric bistable plate for nonlinear broadband energy harvesting. *Appl. Phys. Lett.* **2010**, *97*, 104102. [[CrossRef](#)]
17. Leland, E.S.; Wright, P.K. Resonance tuning of piezoelectric vibration energy scavenging generators using compressive axial preload. *Smart Mater. Struct.* **2006**, *15*, 1413–1420. [[CrossRef](#)]
18. Masana, R.; Daqaq, M.F. Electromechanical Modeling and Nonlinear Analysis of Axially Loaded Energy Harvesters. *J. Vib. Acoust.* **2011**, *133*, 011007. [[CrossRef](#)]
19. Zhu, Y.; Zu, J. A magnet-induced buckled-beam piezoelectric generator for wideband vibration-based energy harvesting. *J. Intell. Mater. Syst. Struct.* **2014**, *25*, 1890–1901. [[CrossRef](#)]
20. Liu, W.; Formosa, F.; Badel, A.; Agbossou, A.; Hu, G. Investigation of a buckled beam generator with elastic clamp boundary. *Smart Mater. Struct.* **2016**, *25*, 115045. [[CrossRef](#)]
21. Zhang, J.; Zhang, J.; Shu, C.; Fang, Z. Enhanced piezoelectric wind energy harvesting based on a buckled beam. *Appl. Phys. Lett.* **2017**, *110*, 103903. [[CrossRef](#)]
22. Jiang, X.; Zou, H.; Zhang, W. Design and analysis of a multi-step piezoelectric energy harvester using buckled beam driven by magnetic excitation. *Energy Convers. Manag.* **2017**, *145*, 129–137. [[CrossRef](#)]
23. Gafforelli, G.; Corigliano, A.; Xu, R.; Kim, S. Experimental verification of a bridge-shaped, nonlinear vibration energy harvester. *Appl. Phys. Lett.* **2014**, *105*, 203901. [[CrossRef](#)]
24. Renaud, M.; Fiorini, P.; van Schaijk, R.; van Hoof, C. Harvesting energy from the motion of human limbs: The design and analysis of an impact-based piezoelectric generator. *Smart Mater. Struct.* **2009**, *18*, 035001. [[CrossRef](#)]
25. Wei, S.; Hu, H.; He, S. Modeling and experimental investigation of an impact-driven piezoelectric energy harvester from human motion. *Smart Mater. Struct.* **2013**, *22*, 105020. [[CrossRef](#)]
26. Tang, Q.C.; Yang, Y.L.; Li, X. Bi-stable frequency up-conversion piezoelectric energy harvester driven by non-contact magnetic repulsion. *Smart Mater. Struct.* **2011**, *20*, 125011. [[CrossRef](#)]
27. Pillatsch, P.; Yeatman, E.M.; Holmes, A.S. A piezoelectric frequency up-converting energy harvester with rotating proof mass for human body applications. *Sens. Actuators A Phys.* **2014**, *206*, 178–185. [[CrossRef](#)]
28. Ramezanpour, R.; Nahvi, H.; Ziaei-Rad, S. A vibration-based energy harvester suitable for low-frequency, high-amplitude environments: Theoretical and experimental investigations. *J. Intell. Mater. Syst. Struct.* **2015**, *27*, 642–665. [[CrossRef](#)]
29. Gu, L.; Livermore, C. Compact passively self-tuning energy harvesting for rotating applications. *Smart Mater. Struct.* **2012**, *21*, 015002. [[CrossRef](#)]
30. Guan, M.; Liao, W.H. Design and analysis of a piezoelectric energy harvester for rotational motion system. *Energy Convers. Manag.* **2016**, *111*, 239–244. [[CrossRef](#)]
31. Febbo, M.; Machado, S.P.; Gatti, C.D.; Ramirez, J.M. An out-of-plane rotational energy harvesting system for low frequency environments. *Energy Convers. Manag.* **2017**, *152*, 166–175. [[CrossRef](#)]
32. Karami, M.A.; Farmer, J.R.; Inman, D.J. Parametrically excited nonlinear piezoelectric compact wind turbine. *Renew. Energy* **2013**, *50*, 977–987. [[CrossRef](#)]
33. Kan, J.; Fan, C.; Wang, S.; Zhang, Z.; Wen, J.; Huang, L. Study on a piezo-windmill for energy harvesting. *Renew. Energy* **2016**, *97*, 210–217. [[CrossRef](#)]
34. Fu, H.; Yeatman, E.M. Rotational energy harvesting using bi-stability and frequency up-conversion for low-power sensing applications: Theoretical modelling and experimental validation. *Mech. Syst. Signal. Process* **2018**, in press. [[CrossRef](#)]
35. Zou, H.X.; Zhang, W.M.; Li, W.B.; Gao, Q.H.; Wei, K.X.; Peng, Z.K.; Meng, G. Design, modeling and experimental investigation of a magnetically coupled flextensional rotation energy harvester. *Smart Mater. Struct.* **2017**, *26*, 115023. [[CrossRef](#)]
36. Xie, Z.; Kitio Kwuimy, C.A.; Wang, Z.; Huang, W. A piezoelectric energy harvester for broadband rotational excitation using buckled beam. *AIP Adv.* **2018**, *8*, 015125. [[CrossRef](#)]
37. Yung, K.W.; Landecker, P.B.; Villani, D.D. An analytic solution for the force between two magnetic dipoles. *Magn. Electr. Sep.* **1998**, *6*, 39–52. [[CrossRef](#)]

